Impact of Horizontal Model Resolution on Mixing and Dispersion in the Northeastern Gulf of Mexico

Nektaria Ntaganou, Eric P. Chassignet, and Alexandra Bozec

Center for Ocean-Atmospheric Prediction Studies (COAPS), Florida State University, Tallahassee, FL 32310

Abstract

In this paper, the importance of model horizontal resolution in identifying the nature of mixing and dispersion is investigated by comparing two data-assimilative, high-resolution simulations (4km and 1km), one of which is submesoscale-resolving. By employing both Eulerian and Lagrangian metrics, upper-ocean differences between the mesoscale- and submesoscale-resolving simulations are examined in the northeastern Gulf of Mexico, a region of high mesoscale and submesoscale activity. The nature of mixing in both simulations is identified by conducting Lagrangian experiments to track the generation of Lagrangian Coherent Structures (LCSs) and their associated transport barriers. Finite-time Lyapunov exponents (FTLE) fields show higher separation rates of fluid particles in the submesoscale-resolving case which indicate more vigorous mixing, with differences being more pronounced in the shelf regions (depths<=500m). The extent of the mixing homogeneity is examined by using probability density functions (PDFs) with results suggesting that mixing is heterogeneous in both simulations, but some homogeneity is exhibited in the submesoscale-resolving case. The FTLE fields also indicate that chaotic stirring dominates turbulent mixing in both simulations regardless of the horizontal resolution. In the submesoscale-resolving experiment, however, smaller scale LCSs emerge as noise-like filaments that suggest a larger turbulent mixing component than in the mesoscale-resolving experiment. The impact of resolution is then explored by investigating the spread of oil particles at the location of the Deepwater Horizon oil spill.

1. Introduction

Beron-Vera (2010) investigated the impact of resolution on Lagrangian transport by mesoscale features by comparing 1/4° altimetry-derived geostrophic velocity data in the Antarctic Circumpolar Current (ACC) to model data at 1/12° horizontal resolution. He argued that higher resolution is essential to further understand the nature of mixing and perform deterministic calculations of Lagrangian transport in highly energetic, eddy-rich regions in the ocean. Specifically, Beron-Vera (2010) showed that the mixing was heterogeneous in both datasets, implying that chaotic advection dominates over turbulent mixing, with more intricate coherent structures being revealed with the increase of resolution. Furthermore, submesoscale processes (0.1-10km) have been shown to be crucial in understanding upper ocean dynamics (McWilliams, 2016), with respect to transport of tracers and mixing (Capet et al., 2008a; Thomas et al., 2008). With advancements in numerical model resolution, as well as increase in observational data availability, these finer-scale processes have been increasingly studied, either solely (Mahadevan and Tandon, 2006; Thomas et al., 2008) or in relation to coexisting mesoscale processes (Capet et al., 2008b, 2008c, 2008b; Liu et al., 2018, 2021; Yang et al., 2021). The importance of understanding the influence of the submesoscale dynamics on the larger picture of the mesoscale lies on the interchangeable character of the respective spatial and temporal scales and on the fact that one cannot exist without the other.

The impact of the submesoscale on Lagrangian transport in the Gulf of Mexico (GoM) was studied in Zhong and Bracco (2013) by comparing a submesoscale-permitting simulation (~1km horizontal resolution) to mesoscale-resolving one (~5km horizontal resolution). They showed that the submesoscale-resolving simulation revealed energetic filaments and accumulation zones due to ageostrophic processes that were not present in the mesoscale-resolving one. Increased submesoscale-permitting horizontal resolution has also been shown to be important for biochemical processes that are better understood with the inclusion of small-scale structures which accompany the larger mesoscale features (Zhong and Bracco, 2013). Submesoscale-permitting simulations also result in larger vertical velocities in the mixed layer as well as higher rates of vertical mixing in the northern and western GoM (Zhong and Bracco, 2013; Liu et al., 2021).

In the present study, we aim to further investigate the value added from resolving those finer scales with respect to Lagrangian transport and mixing. Specifically, we address the question as to whether chaotic stirring still dominates as in Beron-Vera (2010) or if turbulent mixing becomes more important when submesoscale features are resolved. The impact of resolving the submesoscale is quantified using two data-assimilative simulations, at 4km and 1km horizontal resolutions, respectively. In both simulations, the mesoscale fields are constrained by assimilating the same observational data on the 4km grid. In the submesoscale-permitting (1km resolution) simulation, the submesoscale field is, however, allowed to develop and evolve. This is an advantageous set-up, as any differences emerging from the comparison of the two simulations can be directly attributed to the presence of the submesoscale field since the mesoscale fields are constrained in both simulations. In Zhong and Bracco (2013), their simulations only allowed for a statistical approach of the effects of the submesoscale field on Lagrangian transport. Using Eulerian and Lagrangian metrics, the aim is to elucidate the role of the added resolution on the Lagrangian transport and mixing. We focus on the northeastern GoM which exhibits high mesoscale and submesoscale activity (Figure 1) and which is known for biogeochemical importance, especially during the DeepWater Horizon Oil Spill (Liu et al., 2011; Olascoaga and Haller, 2012; Zhong and Bracco, 2013; Poje et al., 2014; Beron-Vera and LaCasce, 2016; Bracco et al., 2016; Liu et al., 2018).

The paper is organized as follows: After a brief overview of the model configurations and the data assimilation approach, the added value of the increased resolution between the two numerical simulations is discussed in Section 2 by comparing model surface velocities from both simulations to surface drifter velocities. Root mean square errors in velocities between the simulations and observational datasets suggest that the error is reduced when the resolution is increased on the scales that are constrained by the assimilated observations, in agreement with Jacobs et al. (2019). Differences in kinetic energy spectra between the numerical simulations indicate that the submesoscale-resolving simulation exhibits higher kinetic energy and flatter spectral slopes as shown by Zhong and Bracco (2013). In Section 3, the impact of the increased resolution on the Lagrangian transport and mixing is analyzed by first performing Lagrangian particle experiments forward and backward in time. The forward in time trajectories are used to calculate particle distributions and compute cumulative and total distances covered. The backward in time trajectories are used to calculate Finite-Time Lyapunov Exponents (FTLEs) and their associated attracting Lagrangian Coherent Structures (LCSs). The FTLE fields and their LCSs show that mixing is more vigorous in the submesoscale-resolving case and the PDFs of FTLEs provide insight on the extent of mixing homogeneity. Similarities in the structure of FTLEs between the simulations suggest that chaotic stirring prevails over turbulent mixing and that LCS-induced mixing is resolution-independent as shown by Beron-Vera (2010) for mesoscale flows. Finally, the impact of resolving submesoscale features is discussed in Section 4 in the context of the 2010 DeepWater Horizon spill, with more oil particles reaching the northern GoM shelf in the submesoscale-resolving case within the span of a month from the release date. A summary and concluding remarks are presented in Section 5.

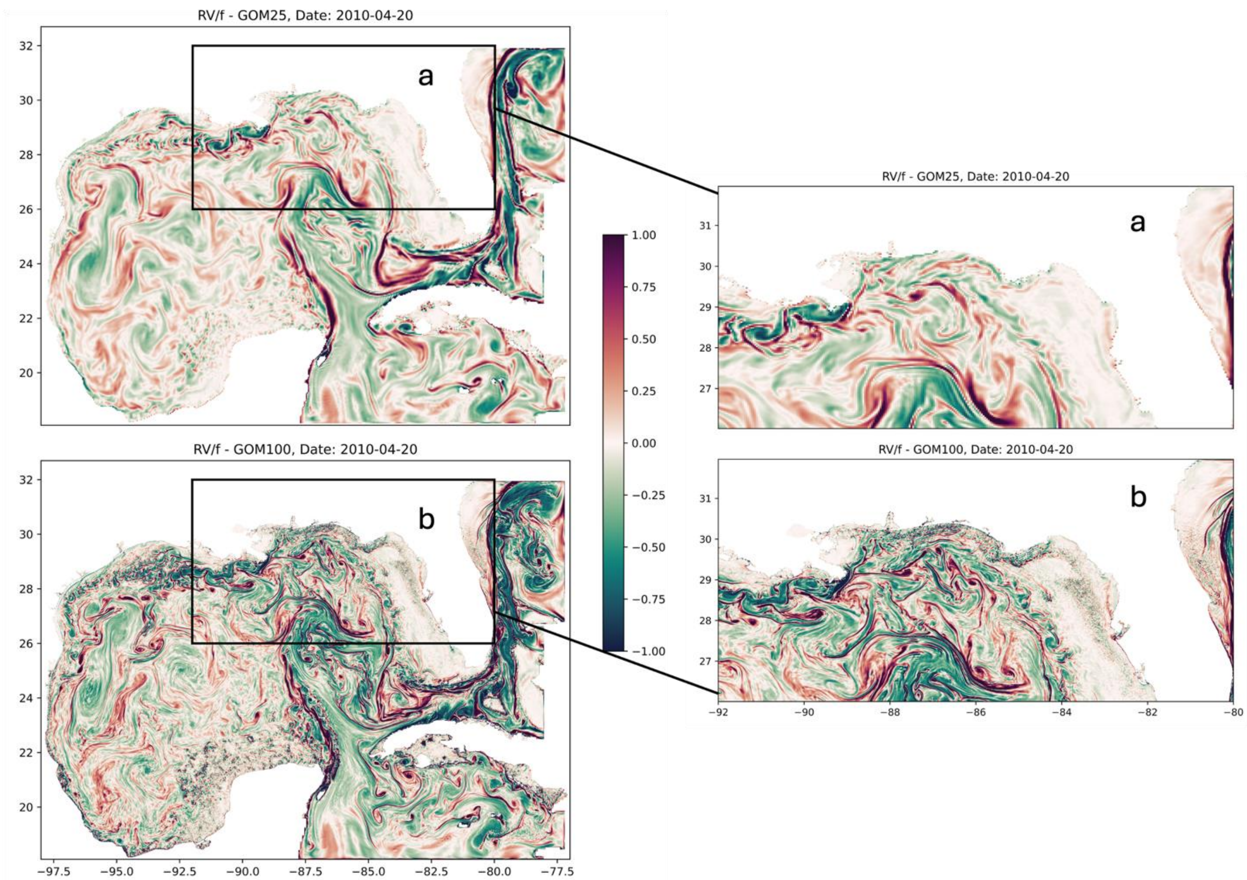

Figure 1: Snapshots of normalized relative vorticity (RV/f) for a) GOM25 and b) GOM100 on April 20, 2010. The black box indicates the region of the northeastern GoM where Lagrangian particle experiments were conducted. A magnified version of the region enclosed by the black box in panels a) and b) is shown in the top right and bottom right panels, respectively.

2. Eulerian comparison of the 1/25°- and 1/100°-resolution hindcast simulations

In this section, we compare a subset of two high-resolution 20+ year reanalyses[1] performed with the Hybrid Coordinate Ocean Model (HYCOM) (Bleck, 2002; Chassignet et al., 2003) applied in the GoM, at 1/25° (~4km) and 1/100° (~1km) horizontal resolution. Details on the numerical model and the hindcasts are provided subsections 2.1 and 2.2, respectively. To demonstrate the value of the increased resolution, an evaluation of the RMS error in model velocities against surface drifter velocities is conducted in subsection 2.3. Finally, in subsection 2.4, we discuss the differences in terms of normalized relative vorticity and kinetic energy spectra (Eulerian metrics).

2.1 Numerical model

The model domain of both configurations extends from 98°E to 77°E in the zonal direction and from 18°N to 32°N in the meridional direction. The vertical resolution consists of 41 hybrid layers and the latest version of the model (2.3.01: https://github.com/HYCOM/HYCOM-src) is forced with hourly Climate Forecast System Reanalysis (CFSR) atmospheric fields from 2001 to 2011 and CFSRv2 fields from 2012 onward. The lateral open boundaries are relaxed to daily means of the global HYCOM GOFS3.1 reanalysis (https://www.hycom.org/dataserver/gofs-3pt1/reanalysis). Tidal forcing with five tidal constituents (M2, S2, O1, K1, N2) is applied at the surface through a local tidal potential and at the boundaries with Browning-Kreiss boundary conditions. The tidal data are extracted from the Oregon State University (OSU) TPXO9 atlas (Egbert and Erofeeva, 2002). The same high resolution 1km GoM bathymetry of Velissariou (2014) is used to generate the bathymetry for the 1/25° and 1/100° domains. is derived from the same bathymetry but interpolated on the 1/25° grid.

2.2 Data assimilation

Both configurations are data-assimilative and the hindcasts are produced with the use of the Tendral Statistical Interpolation (T-SIS) package (Srinivasan et al., 2022; www.tendral.com/tsis). The basic functionality of the package is a multivariate linear statistical estimation given a predicted ocean state and observations. To optimize the system's performance for the HYCOM Arbitrary-Lagrangian-Eulerian (ALE) vertical coordinate system, subsurface profile observations are first re-mapped onto the model hybrid isopycnic-sigma-pressure vertical coordinate system

[1] Available at https://www.hycom.org/dataserver/gom/gom-reanalysis

prior to assimilation. The analysis procedure then updates each coordinate layer separately in a vertically decoupled manner. A layerized version of the Cooper and Haines (1996) procedure is used to adjust model layer thicknesses in the isopycnic-coordinate interior in response to SSH anomaly innovations. Prior to calculating SSH innovations, a mean dynamic topography (MDT) derived from a 20-year free-run of the GOMb0.04 configuration is added back into the altimetry observations. The multi-scale sequential assimilation scheme based on a simplified ensemble Kalman Filter (Evensen, 2003; Oke et al., 2002) is used to combine the observations and the model to produce best estimates of the ocean state at analysis time. This state is then inserted incrementally into HYCOM over 9 hours. The analysis is done daily at 18Z.

In the 1/100º configuration, since the resolution of the observations that are fed to the TSIS assimilation system is not high enough compared to the grid resolution, the analysis is performed on the 1/25º grid. The 1/100º ocean state is first box-car averaged at 1/25º to remove the small-scale variability and given to TSIS as the ocean state. The assimilation system then performs the reanalysis at this resolution and provides an increment that is then interpolated back at the 1/100º grid and added to the 1/100º configuration ocean state.

The TSIS assimilative system accepts Sea Level Anomaly (SLA), Sea Surface Temperature (SST), and T/S profiles. For the hindcasts used in the present study, remotely sensed SLA and SST were assimilated, as well as in-situ T/S, which are considered to be the most reliable observations. Along-track SLA from four operational satellite altimeters (T/P, Jason 1,2, Envisat, GFO and Cryosat) constitute the most important dataset for constraining the model. The data are available from Collecte Localisation Satellites (CLS) from January 1993 to present (https://www.aviso.altimetry.fr/). These data are geophysically corrected for tides, inverse barometer, tropospheric, and ionospheric signals (Le Traon and Ogor, 1998; Dorandeu and Le Traon, 1999). For the sea surface temperature, we use the SST (Foundation Temperature) Level 4 product from NAVOCEANO (GHRSST) (https://podaac.jpl.nasa.gov/GHRSST) and NOAA/NODC (AVHRR) (https://www.ncdc.noaa.gov/oisst/optimum-interpolation-sea-surface-temperature-oisst-v21) which integrates several individual sensors and provides a gridded field with error estimates. ARGO floats (https://argo.ucsd.edu) are also used to constrain the sub-surface density structure when available over the hindcast period.

2.3 Comparison to observed GoM surface drifter velocities

To quantify the added value of the increased horizontal resolution, we compare the model velocity fields from both simulations to velocities derived from drifter trajectories over the whole GoM. From now on, we will be referring to the GoM-HYCOM 1/25° configuration as "GOM25" and to the GoM-HYCOM 1/100° configuration as "GOM100". We use the freely available drifter dataset "GulfDriftersOpen", details of which can be found in Lilly and Pérez-Brunius (2021). The authors gathered all publicly available drifter data in the GoM, compiled, and made them available in a single user-friendly dataset that includes drifter interpolated hourly positions and velocities from 1992 to 2020.

We select velocities from drifters with a drogue, as undrogued drifters trajectories are impacted by surface winds and waves. Three independent sets of drifters types are used: CODE (Davis, 1985), CARTHE (Novelli et al., 2017), and SVP (Lumpkin and Pazos, 2007). The CODE and CARTHE drifters have a 1m drogue while the SVP drifters have a 15m drogue. The tracking system of the drifters can be either Argos or GPS. Drifters before 2013 are Argos-tracked with positioning errors up to hundreds of meters (Elipot et al., 2016) and drifters after 2013 are GPS-tracked, with much higher positioning accuracy (a few meters) than the Argos-tracked. Consequently, only GPS-drifters are able to resolve small-scale motions such as submesoscale eddies and waves (Lilly and Pérez-Brunius, 2021). Thus, in this study, we only use GPS-tracked, same-type drifters to compare with the model outputs for the time periods when available drifter data overlap with the model outputs (2013 to 2020).

The three different types of drifters used in the analysis were deployed for various experiments over the time period of interest (2013-2020). The CODE drifter data used for the present analysis come from the Grand Lagrangian Deployment (GLAD; Poje et al. 2014) experiment initiated by the Consortium for Advanced Research on Transport of Hydrocarbon in the Environment (CARTHE). In total, there are ~300 CODE drifter trajectories coming from the GLAD experiment (Figure 2, left panel). Since the GLAD experiment was designed to study dispersion in the GoM (Poje et al., 2014), the drifters were deployed for a relatively short period of time and their trajectories mostly cover the eastern part of the GoM. The CARTHE drifters were deployed for the LASER (The Lagrangian Submesoscale Experiment - Haza et al., 2018; Özgökmen et al., 2018) experiment. There are ~1300 LASER trajectories between January and March of 2016 covering a large portion of the GoM (Figure 2, middle panel). The SVP drifters were deployed as part of the GDP (Global Drifter Program;

https://www.aoml.noaa.gov/phod/gdp/index.php) that started in September 1996. 44 SVP drogued drifter trajectories are available after 2013 (Figure 2, right panel). A review of all the drifter deployments mentioned here can be found in Lilly and Pérez-Brunius (2021) and references therein. We point out that drifter locations at all depths are used in our analyses, which might account for some larger errors due to shelf dynamics being dependent on topographic effects. The inertial period is also not removed, which could increase the error due to wind forcing (Jacobs et al., 2019).

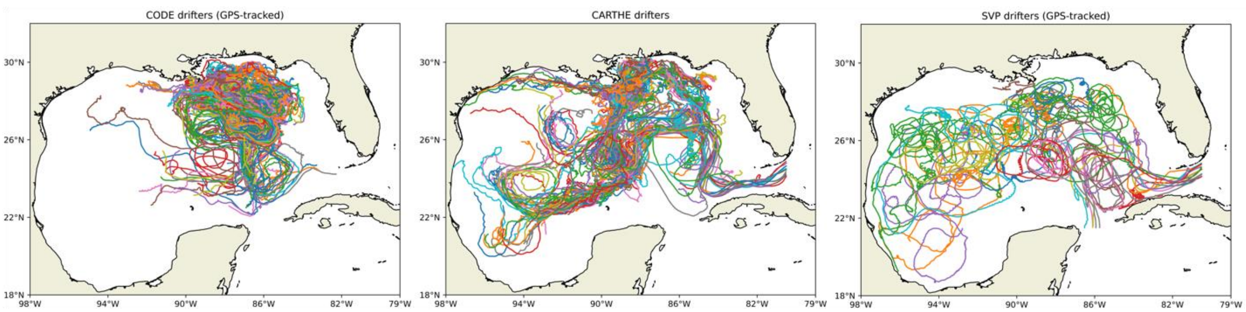

Figure 2: Trajectories from CODE (left), CARTHE (middle), and SVP (right) drifters after 2013 for all the relevant experiments mentioned in Section 3.

The Root Mean Square errors (RMSEs) between velocities from the numerical experiments and the CODE, CARTHE, and SVP, drifters are shown in Figure 3. In all cases, the neared model neighbor to the drifter's position is used to compute the RMSE. In general, GOM100 does not exhibit reduced errors (Figure 3, red lines) when compared to GOM25 (Figure 3, blue lines). In fact, in almost all cases, the error values of GOM100 and GOM25 compared to drifter velocities are either very similar or slightly higher in GOM100. This is because of the gap in the resolved scales between the observations that are assimilated in the model, that primarily come from satellite altimeters, and the model itself (D'Addezio et al., 2019; Jacobs et al., 2019; Jacobs et al., 2021). Higher resolution models, especially submesoscale-resolving, can produce higher errors and seemingly show less skill when compared to mesoscale-resolving ones (D'Addezio et al., 2019; Jacobs et al., 2019). The lack of RMS error improvement with an increase of the model resolution raises the question as to whether higher horizontal resolution is actually useful with respect to model skill. Jacobs et al. (2019) addressed that question by deconstructing the fields into constrained and unconstrained scales in order to filter the unconstrained small-scale variability present in their high-resolution forecast model and evaluate model skill. Constrained scales are defined as the scales at which the model is constrained by the observations assimilated.

The scales that are not constrained by observations (small-scale variability) are defined as the unconstrained scales. Jacobs et al. (2019) ran several experiments of their model with different decorrelation scales to establish which decorrelation scale minimized the errors when compared to drifter trajectories from the LASER experiment. They then deconstructed the surface velocity field into constrained and unconstrained scales using a Gaussian convolution kernel with different length scales that were also compared against the drifter trajectories. They concluded that the lowest errors were produced using a decorrelation scale of 36km and a Gaussian convolution kernel with an e-folding scale of 58km.

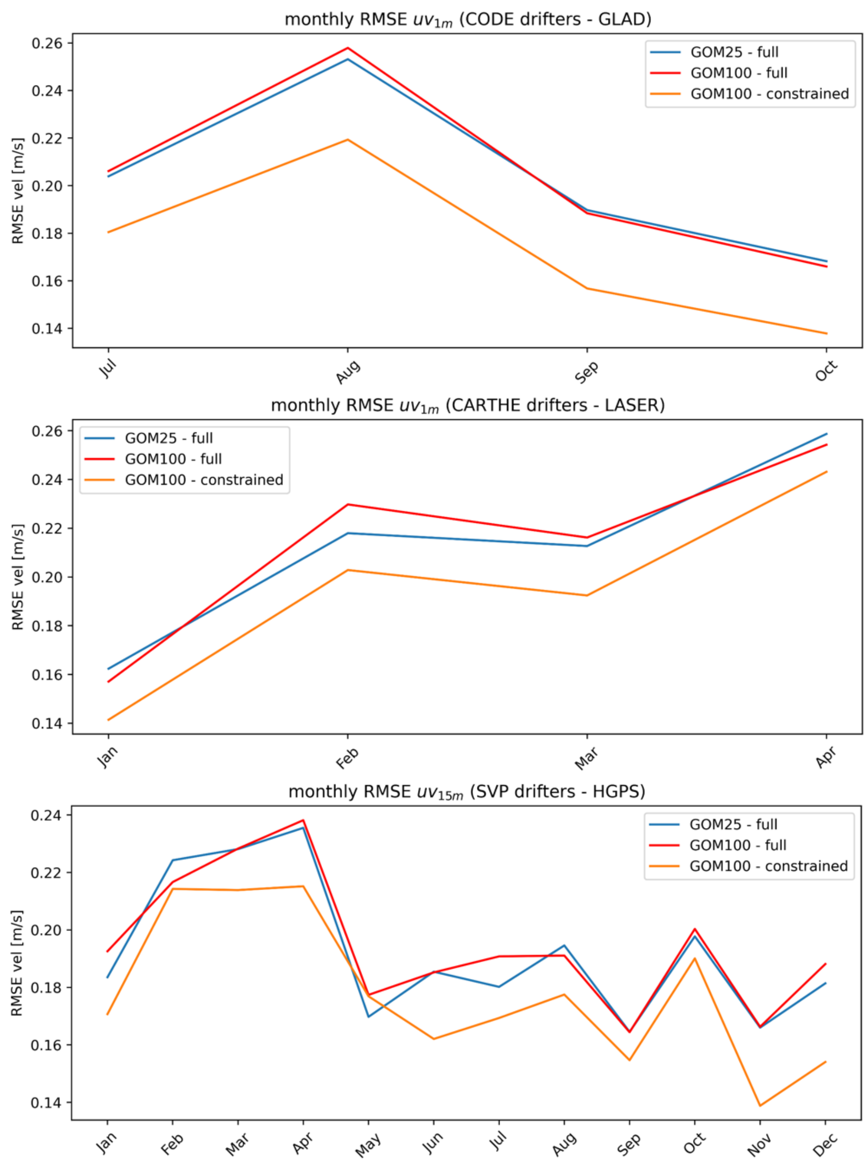

Figure 3: Full velocity RMSE between the drifter and model outputs for GOM25 (blue), GOM100 (red), and the constrained values of GOM100 (orange) for three drifter types: and CODE drifters from the GLAD experiment (top panel), CARTHE drifters from the LASER experiment (middle panel), and SVP drifters (bottom panel).

Following their example, we use a Gaussian convolution kernel to filter out the small scales of GOM100 velocity field with a standard deviation of 30km which roughly corresponds to an e-folding scale of 60km. The main purpose is to determine how the RMSE from GOM25 compares to the RMSE from GOM100 using the same independent observations to support the hypothesis that the information extracted from the GOM100 simulation is credible. Such is possible by demonstrating that even though the total RMSE from GOM100 shows little to no improvement, it can in fact, be reduced if the unconstrained scales are filtered out. The results are shown in Figure 3 (orange lines) for all different drifter types that were described earlier in this subsection. For the CODE and CARTHE drifters, the errors of the constrained model fields in GOM100 are reduced everywhere after filtering out the small scales when compared to the full-field errors of both GOM100 and GOM25. A similar result is obtained with the SVP drifters from the GLAD experiment, with the exception of just 1 point where the constrained GOM100 field error is slightly larger than its GOM25 full-field counterpart. This deviation, however, is minimal, and our results therefore confirm the results put forward by Jacobs et al. (2019). As further argued in Jacobs et al. (2021), the scales that are constrained by observations have deterministic predictive skill, whereas the unconstrained scales have statistical predictability, as they contain the majority of forecast errors. Therefore, we can state that there is value in progressing toward and exploring higher resolution models, as both constrained and unconstrained scales contribute to a better representation of the ocean state. Scales constrained by observations provide low-error information on the large scale and mesoscale circulation and scales in the unconstrained bands yield information on small-scale variability and errors that are important as submesoscale features are directly related to their mesoscale counterparts.

2.4 Kinetic energy spectra

As shown in Figure 1b, there is an abundance of small-scale structures in the entire GoM, both cyclonic and anticyclonic, pointing toward a submesoscale signature that is evident in GOM100, but not in GOM25. These structures are much smaller on the shelf regions and frontal structures that are evident in GOM25 (i.e., West Florida Shelf, Figure 1a) are thinner and accompanied by small-scale eddies in GOM100 (i.e., West Florida Shelf, Figure 1b). Small-scale structures are also evident around the Loop Current Eddy (LCE) and on the Loop Current (LC) front. The submesoscale regime often develops around mesoscale eddies and frontal jets, in the form of smaller eddies or sharp fronts and filaments (D'Asaro et al., 2011; McWilliams, 2016; Bracco et al., 2019). Submesoscale eddies form primarily due to mixed-layer instabilities (Molemaker et al., 2005) or frontogenesis (Capet et al., 2008c). A unique aspect of this comparison is that the mesoscale features are constrained in both GOM25 and GOM100 via data assimilation (see section 2.2), but that submesoscale activity is free to develop in GOM100. This allows us to state that the observed differences in advection and diffusion are primarily due to the submesoscale and not a different representation of the mesoscale. In the northeastern GoM (see black box, Figure 1), the submesoscale activity in GOM100 is quite pronounced, with both small eddies and sharp fronts. In this region, the submesoscale circulation is strongly affected by the freshwater input from the Mississippi river and is, in fact, intensified because of the frontogenesis induced by the sharp density gradients in salinity (Poje et al., 2014; Luo et al., 2016; Barkan et al., 2017a).

The increase in model resolution also modifies the spatial distribution of kinetic energy, as there is a large increase of energy in scales smaller than 50km in GOM100 both in winter (January, February, March) and summer (July, August, September) (Figure 4). The differences in kinetic energy grow larger as the scales become smaller with the spectral slopes in GOM100 (~-2) being flatter when compared to GOM25 (~-3) during both seasons. Slope values of -3 and steeper are representative of mesoscales and geostrophic flows (Zhong and Bracco, 2013) while kinetic energy spectra with slope values shallower than -3 are typical of submesoscale circulations based on horizontal model resolutions of 1-2km (Capet et al., 2008a; Klein et al., 2008; Zhong and Bracco, 2013; Barkan et al., 2017b).

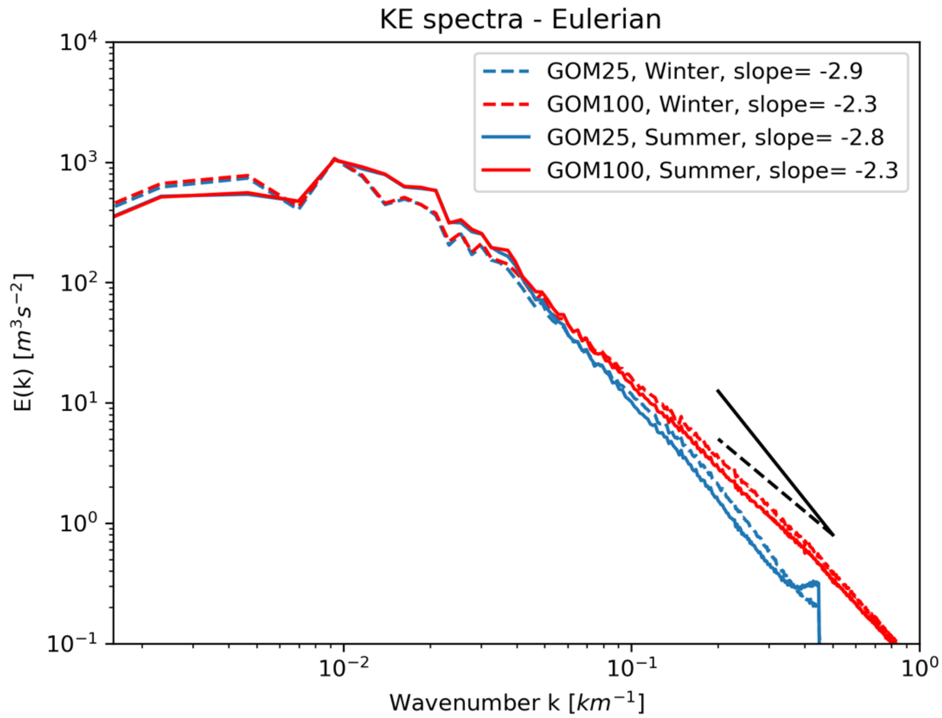

Figure 4: Kinetic energy spectra for the entire GoM region in winter (dashed blue and red) and summer (solid blue and red) of 2010 for GOM100 (red) and GOM25 (blue) experiments. The black lines represent the -3 (solid) and -2 (dashed) spectral slopes.

3. Lagrangian transport and mixing in the northeastern GoM

The previous section described and compared the two experiments from an Eulerian point of view. In this section, we investigate the impact of resolution on Lagrangian transport and mixing in the northeastern GoM (black box, Figure 1), one of the regions in the GoM characterized by high submesoscale activity (Figure 1b) and the location of the 2010 DeepWater Horizon oil spill. As shown in Figure 1, the 1km configuration (GOM100, Figure 1b) exhibits a lot of small-scale eddies and fronts (the submesoscale soup as described by McWilliams 2016) that are not present in GOM25 (Figure 1a).

3.1 Experimental setup

The first step in a Lagrangian framework approach is to generate Lagrangian particle trajectories. This was achieved by using the OceanParcels Lagrangian Framework toolbox (Delandmeter and Van Sebille 2019, https://oceanparcels.org/) and seeding 2-d passive particles in the northeastern GoM that are advected at the ocean surface with a 4th order Runge-Kutta advection scheme (dt=2h). We performed two sets of experiments, one forward and one backward in time, each of them with 2,250,000 particles released on a 1500x1500 grid (see location in Figure 1) spaced 500m in the x-direction and 1000m in the y-direction. The hourly surface velocities used to advect the particles are from GOM25 and GOM100, respectively (see Subsection 2.1) for the full 2010 year, the year of the Deepwater Horizon oil spill. Each forward-time release was repeated every 10 days and integrated forward for 3 months. The forward-time trajectories are used to calculate particle distributions and compute cumulative and total distances covered. Each backward-time release was repeated every 10 days and integrated backward for 10 days. The backward-time generated trajectories are used to identify transport barriers and attracting Lagrangian Coherent Structures (LCSs) by calculating finite-time Lyapunov exponents (FTLEs).

3.2 Example of Lagrangian trajectories

An example of particle positions for one of the forward-time releases is presented in Figure 5 for a release on May 1, 210. The differences in trajectories between the two simulations illustrate the impact of resolving the submesoscale in GOM100. Overall, the particle distribution is more diffused around the constrained mesoscale features in GOM100 than in GOM25. The biggest difference is found in the easter GoM, especially over the West Florida Shelf. In GOM25, the particles are distributed all over the shelf while, in GOM100, they have the tendency to cluster along one line in the north-south direction. The cumulative distances of the particles from the forward-time releases are quite similar in both simulations with only the medians in GOM100 being ~10% higher when compared to GOM25 (not shown). The small differences in cumulative distances can be attributed to higher frequency motions resulting from the submesoscale activity of GOM100.

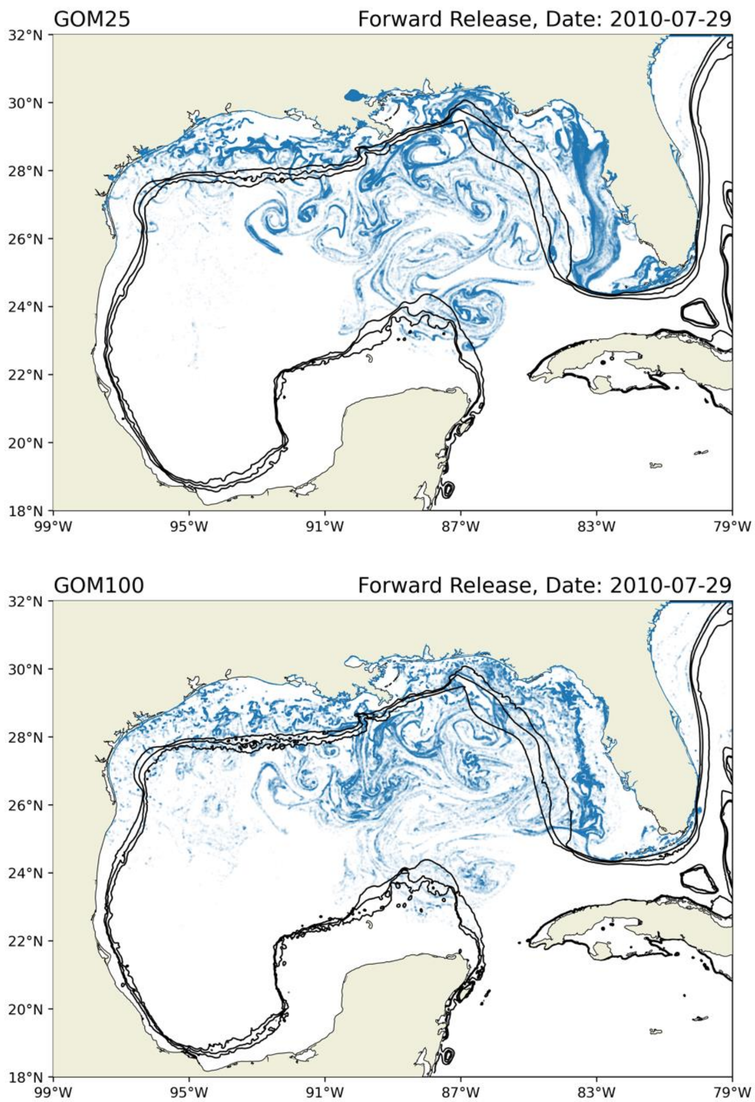

Figure 5: Particle positions at the end of a 90-day forward-time release in the northeast GoM (black box in Figure 1) and initiated on May 1, 2010 - GOM25 (top) and GOM100 (bottom).

3.3 Finite Time Lyapunov Exponents (FTLEs)

FTLEs measure the separation rate of nearby fluid particles in the time interval $\tau = t - t_0$, where t_0 and t are the initial and final positions of the fluid particles, respectively. FTLE is defined as

$$\sigma_t^\tau(x) \coloneqq |\tau|^{-1} ln\lambda_{max}(\Delta(x;t,\tau))$$

where λ_{max} is the maximum eigenvalue of the right Cauchy-Green deformation tensor $\Delta(x;t,\tau)$ which is defined as

$$\Delta(\mathrm{x};\mathrm{t},\tau) \coloneqq \partial_x \varphi_t^{t+\tau}(\boldsymbol{x})^T \partial_x \varphi_t^{t+\tau}(\boldsymbol{x})$$

where $\varphi_t^{t+\tau}(\boldsymbol{x})$ is the flow map defined as $\varphi_t^{t+\tau}: \boldsymbol{x}(t) \longmapsto \boldsymbol{x}(t+\tau)$, where $\boldsymbol{x}(t)$ is the position of the fluid particles at time t. The flow map $\varphi_t^{t+\tau}(\boldsymbol{x})$ is calculated by integrating the particle trajectories from $t = t_0$ to $t = t + \tau$. FTLEs represent the maximal rate of mixing (stretching/folding) about the particle trajectory and can be calculated either in forward ($\tau > 0$) or in backward time ($\tau < 0$). Ridges of FTLE's are indicators of Lagrangian Coherent Structures (LCSs) (Haller, 2002; Shadden et al., 2005). Ridges of forward-time FTLEs identify repelling LCSs, whereas ridges of backward-time FTLEs indicate attracting LCSs (for a schematic illustration, see Farazmand and Haller, 2013). However, both attracting and repelling LCSs can be identified from a single chunk of data (without selecting from forward- or backward-time calculations) by calculating the maximum and minimum eigenvectors of the Cauchy-Green tensor (Farazmand and Haller, 2013). Repelling LCSs are a metric for maximal local stretching, while attracting LCSs are linked to regions where oceanic passive tracers accumulate (Beron-Vera et al., 2008; Beron-Vera, 2010; Olascoaga and Haller, 2012; Farazmand and Haller, 2013). LCSs are surfaces of local FTLE maxima or curvature ridges of the FTLE field (Shadden et al., 2005). As shown in Shadden et al. (2005), to extract the LCSs, we first need to define the curvature of the FTLE field, given by the Hessian matrix Σ. Hessian matrix is a square matrix of second order partial derivatives of a scalar function, such as the FTLE and determines points of local maxima and minima. Σ is defined as:

$$\Sigma := \frac{d^2 \sigma_t^{t+\tau}(\boldsymbol{x})}{d\boldsymbol{x}^2}$$

where σ is the FTLE field. To, then, identify a curvature ridge (second-derivative ridge), the smallest eigenvalue of Σ, λ_n and its eigenvector $\boldsymbol{n}$ need to satisfy the following conditions:

$\lambda_n < 0$ and $\nabla\sigma \cdot \boldsymbol{n} = \boldsymbol{0}$ (vectors $\nabla\sigma$ and $\boldsymbol{n}$ must be parallel)

When these conditions are met, they define a curve that moves in time, i.e. the LCS. Since we are interested in identifying regions of passive particle convergence, we will be focusing on backward-time FTLE calculations with $\tau = -10$ days and attracting LCSs. The attracting LCSs stem from advective mixing and characterize regions of accumulation (Haller, 2001a; Beron-Vera, 2010; Allshouse and Peacock, 2015; M. P. Perez et al., 2020). The chosen time interval of 10 days allows us to capture short-lived finer-scale patterns (Sinha et al., 2019).

The FTLE calculations are conducted with the purpose of identifying possible changes in transport barriers and the nature of mixing in the northeastern GoM as the model resolution increases from 4km to 1km. FTLEs provide a description of how mixing and transport is organized around the transport barriers that are marked by the FTLE ridges (Haller and Yuan, 2000; Shadden et al. 2005). Shadden et al. (2005) also showed that the flux of FTLEs along the Lagrangian ridges is minimal, proving that they are almost material lines. The notion of material lines, extensively discussed in the theory of dynamical systems, denotes a flow barrier that distinguishes fluids with different properties. Finally, it is important to note that an FTLE field is of a diagnostic nature in terms of mixing and does not give information on the features of the velocity field that was used to generate the particle trajectories (Haller, 2001b).

3.4 Chaotic advection versus turbulent mixing

To further investigate the differences in Lagrangian transport between the two data assimilative numerical simulations, we performed backward-time particle experiments conducted every 10 days for one year starting on January 1st, 2010. The simulated trajectories are used to calculate FTLEs and the associated LCSs, snapshots of which are shown in Figure 6. The snapshots provide an example of a winter distribution (Figures 6a-d) and of a summer one (Figures 6e-h) which are representative of the Lagrangian picture throughout the entire year, as will be discussed later in this section.

In the winter month example, the FTLE fields and respective LCSs in GOM25 (Figures 6a-b) reveal a plethora of eddy structures that are present in the entire region with smaller scale eddies consistently appearing in the shelf regions. A similar picture is present in GOM100 (Figures 6c-d), but more convoluted than in GOM25. Thus, an abundance of LCSs is also prevalent in GOM100 (Figure 6d), but of smaller scales and covering a much larger area when compared to GOM25 (Figure 6b). Overall, the smaller structures that emerge in GOM100 follow the patterns of GOM25, indicating that the submesoscale in GOM100 is allowed to evolve within the larger mesoscale picture as depicted in GOM25. In the summer month example, in both GOM25 and GOM100, the mesoscale fields are more elongated and there are more frontal structures (Figures 6e-6h). This is consistent with Choi et al. (2017) and Bracco et al. (2019) who documented the appearance of fronts in summer and eddies in winter in the northern GoM. Finally, the FTLE fields are smoother in summer than in winter, in both GOM25 and GOM100.

The seasonality in scales up to 10 km can be attributed to the submesoscale field to intensify in the winter and weaken in the summer (Bracco et al., 2019). The mixed layer instabilities behind the generation of submesoscale features grow in the winter when the mixed layer is deep and weaken during the summer when the mixed layer is shallower (Bracco et al., 2019; Callies et al., 2015; Thompson et al., 2016). For scales larger than 10km, mixed layer instabilities do not exhibit a strong seasonal cycle (Callies et al., 2015). Evidence of eddies and fronts smaller than 10km is shown in the FTLE fields of both GOM25 and GOM100 as the computation of FTLE is not bound by the velocity field resolution (Beron-Vera, 2010).

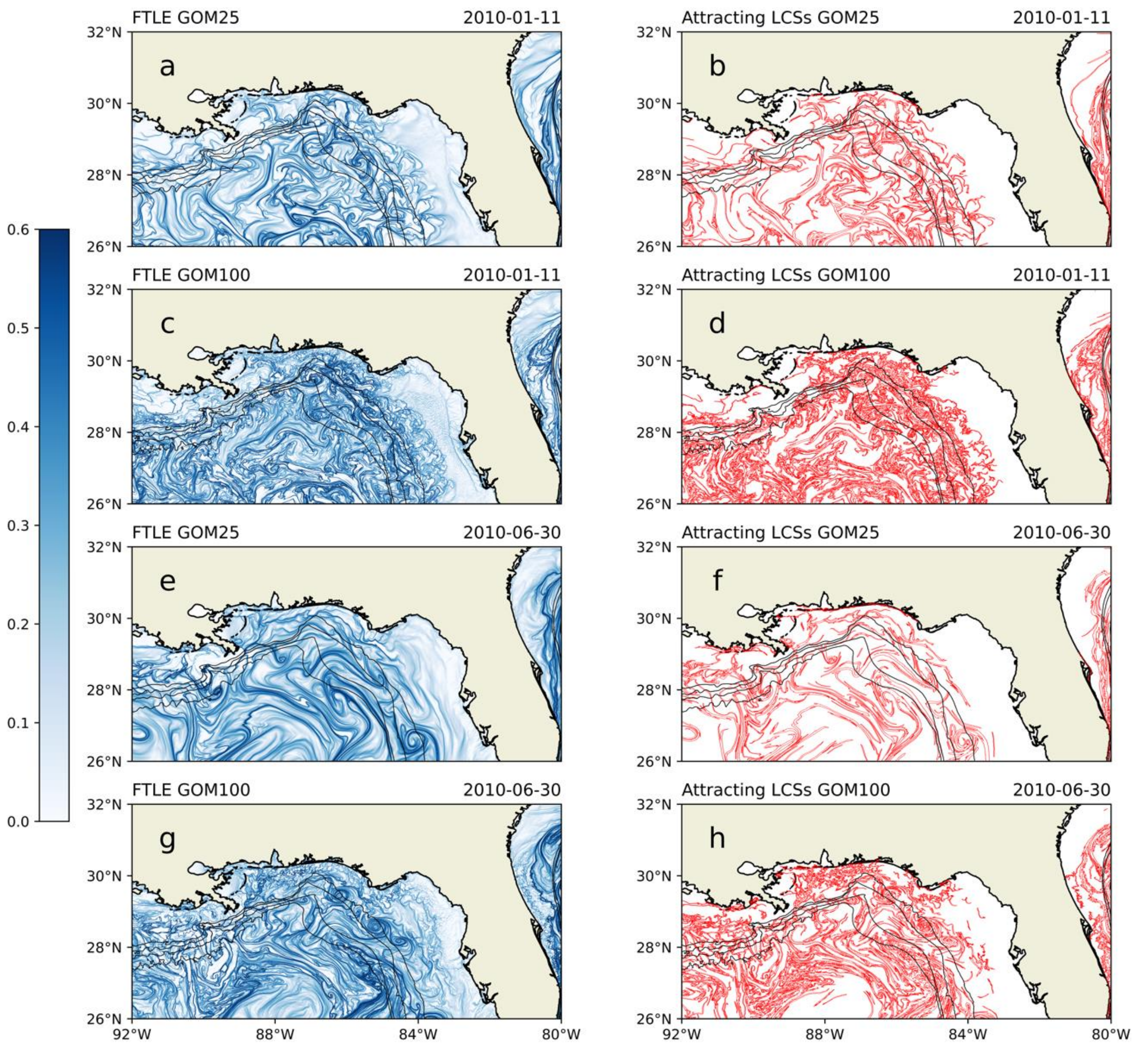

Figure 6: Backward-time normalized FTLE fields and attracting LCSs for two 10-day time intervals ending on 2010-01-11 in (a)-(d) and 2010-06-30 in (e)-(h). Panels (a), (c), (e), and (g) show the normalized FTLE fields, and panels (b), (d), (f), and (h) show the attracting LCSs

extracted from the respective FTLE fields. The solid black lines represent the 100m, 200m, 500m, and 1000m-isobaths, respectively.

Similarly to the winter case, in GOM100 (Figure 6g-h), ridges of FTLEs lie within the larger mesoscale picture of GOM25 (Figures 6e-f). In both experiments and regardless of the season, the increased amount and intricacy of LCSs as well as the higher FTLE values in GOM100 further indicate that the mixing produced by GOM100 velocity fields is more vigorous. Both FTLE fields and LCSs show spiral-like and mushroom-like patterns which indicate eddies (either cyclonic or anticyclonic) and eddy dipoles, respectively (Beron-Vera et al., 2008). An example of a mushroom-like pattern is shown in GOM25 on the West Florida Shelf ~27°N and 84°W (Figures 6a-b). Three consecutive spiral-like patterns are also present in the GOM100 also along the West Florida Shelf between 27°N and 29°N. Overall, more intricate LCSs are produced in GOM100 and higher FTLE values (bolder colors) indicate transport barriers that are more intense in the submesoscale-resolving simulation.

The comparison of FTLE fields between the two simulations also provides some information on as to whether chaotic mixing dominates over turbulent mixing or vice versa. Chaotic mixing or advection is related to mixing by organized invariant manifolds or Lagrangian coherent structures (Brown and Smith, 1991; Pierrehumbert, 1991; Koshel' and Prants, 2006; Budyansky et al., 2007; Beron-Vera and Olascoaga, 2009; Beron-Vera, 2010). Turbulent mixing is related to incoherent and irregular flow, whereas chaotic advection refers to quasi-irregular flow. In both cases (winter and summer), the FTLE fields clearly show similarities with respect to the larger mesoscale picture, meaning that in the higher resolution GOM100 simulation, smaller-scale coherent structures emerge within the larger mesoscale picture characterized by GOM25. Thus, the generation of transport barriers is, to a large extent, independent of the resolution. In this set of experiments, we therefore find that the mixing related to LCSs is resolution-independent as it manifests in both resolutions in the form of LCSs. If ocean mixing was resolution-dependent, then the Lagrangian calculations would not display transport barriers or LCSs, and the mixing would be deemed turbulent. This resolution-independent result implies that chaotic mixing is dominant over turbulent mixing. However, the small-scale, noise-like filaments present in Figures 6b and 6f suggest that the component of turbulent mixing is more prevalent in GOM100 than in GOM25 and therefore exhibit some resolution dependence.

There is a larger number of particles accumulating on FTLE ridges or LCSs in GOM100 than in GOM25 (Figure 7), a result associated with stronger Lagrangian transport and mixing in GOM100. More specifically, in GOM100, the percentage of LCS particles (red bars, Figure 7) is persistently higher than in GOM25 (blue bars, Figure 7), a result that is in agreement with the discussion of Figure 6. This further supports the hypothesis that the northeastern GoM is more energetic in the high-resolution simulation, even in a region away from the LC body. Overall, there is a median of ~50% increase in LCS particles in GOM100 over GOM25 in both the entire northeastern GoM and shelf regions with depths<=500m (Figure 8). However, the range of the increase is higher on the shelves when compared to the entire region. Consequently, the shelf regions exhibit the largest differences with more particles organizing themselves along attracting material lines, indicating that shelf dynamics are more energetic in GOM100 than in GOM25. Such a result underlies the importance of shelf dynamics on mixing in the GoM, especially in the West Florida Shelf (Yang et al., 1999; Olascoaga et al., 2006; Beron-Vera and Olascoaga, 2009; Olascoaga, 2010; Choi et al., 2017), and on applications such as oil spill simulations and bio-geochemical modeling.

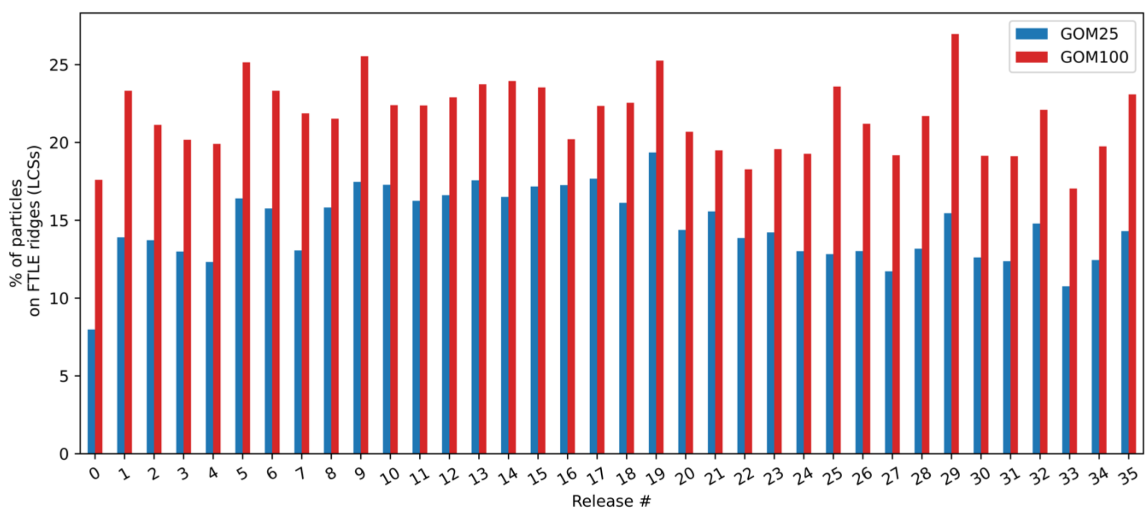

Figure 7: Percentage of particles that ended up on FTLE ridges for all backward-time particle releases in 2010 for GOM25 (blue) and GOM100 (red).

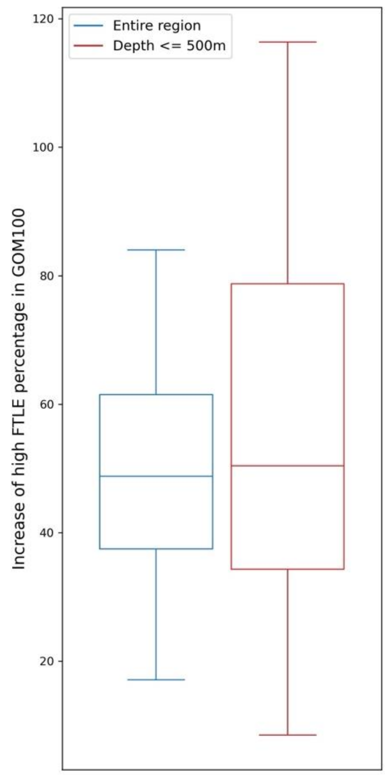

Figure 8: Boxplots of increase of particles that end up on FTLE ridges in GOM100 compared to GOM25 in the entire region (blue) and shelf regions with depths <= 500m (red) .

The PDFs of FTLEs for both GOM25 and GOM100 are positively skewed with long tails toward the shorter time scales with GOM100 exhibiting a longer tail (Figure 9). The longer tail indicates the presence of intense and short-lived events, such as the presence of submesoscale eddies that form and dissipate over a short time period. The asymmetry of the PDFs further implies that chaotic mixing dominates turbulent mixing as discussed earlier. The PDFs would be symmetrical if the situation was reversed, i.e. dominant turbulent mixing. The PDF of the GOM100 FTLE fields is slightly less skewed than GOM25 case, suggesting that the influence of turbulent mixing is slightly larger in GOM100. The heterogeneity of the particle mixing at the surface therefore supports the hypothesis that there is value-added in the increased resolution and the lack of multiple extrema in the PDFs suggests that persistent features are not presents and most of the features are short-lived or transient (Beron-Vera and Olascoaga, 2009). Similar results were produced by Waugh and Abraham (2008) for the global ocean, Beron-Vera (2010) in the Agulhas and ACC regions using altimetry-derived currents, and Beron-Vera and Olascoaga (2009) in the West Florida Shelf using HYCOM outputs.

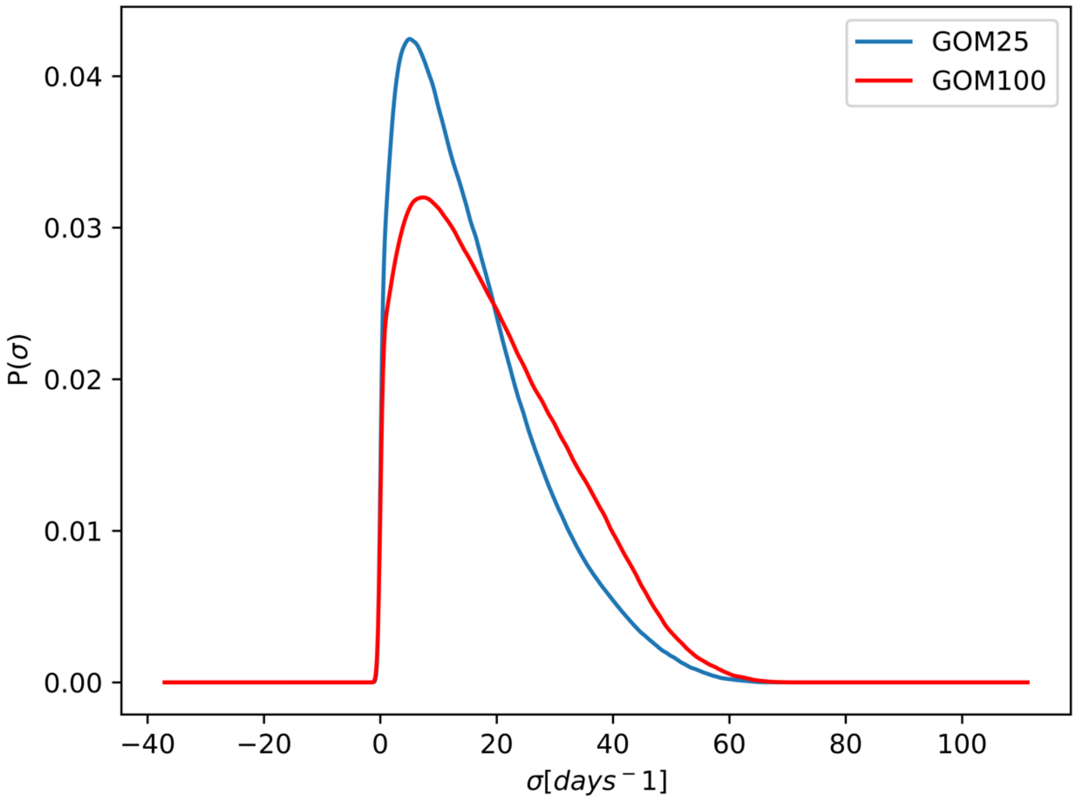

Figure 9: PDFs of backward-time FTLEs for all 10-day particle releases in 2010 for GOM25 (blue) and GOM100 (red). The skewness values are 0.97 for GOM25 PDF and 0.65 for GOM100.

4. Oil particle simulations

Among the variety of applications that could benefit from this study are oil spills with respect to differences in the modeling of oil particle dispersion based on the velocity field horizontal and/or vertical resolution. To illustrate this, two experiments were conducted to provide an initial estimate of differences in oil particle spread as a function of the numerical model's horizontal grid spacing. We use Openoil[2], a 3D oil drift module for oil particle advection and oil spill simulation, distributed by Opendrift[3].

The two examples, shown in Figure 10, were initialized at the location of the Deepwater Horizon spill (28.7°N, 88.4°W) and conducted for one month, using surface velocity fields from

[2] https://opendrift.github.io/autoapi/opendrift/models/openoil/index.html

[3] https://opendrift.github.io/index.html

GOM25 and GOM100 in April-May 2010 and the oil weathering calculations use the NOAA-ERR_ERD OilLibrary package. This package uses the NOAA database for oil droplet densities based on the oil types that are selected for the experiments and calculates oil evaporation and emulsification in the simulations. Starting on April 22, 2010, 1000 oil particles were released at the surface in a 5km radius and tracked until the end of May 2010. Differences in the oil particle positions between the high and low resolutions are clearly visible after one month of integration. More oil particles in the high-resolution 1km GOM100 reach shallow waters than in the 4km GOM25. Furthermore, approximately 30% more GOM100 oil particles end up stranded on land when compared to the GOM25 particles. This is a preliminary experiment to illustrate the impact of small-scale ocean features on oil dispersion. To simulate realistically the Deepwater Horizon oil spill, one would need to include more features such as a plume model, 3D advection, etc. In the case of an oil spill, calculations of FTLE fields in ocean forecasts would provide guidance to first responders on where one may be able to track accumulation of oil as oil particles tend to organize themselves along material lines.

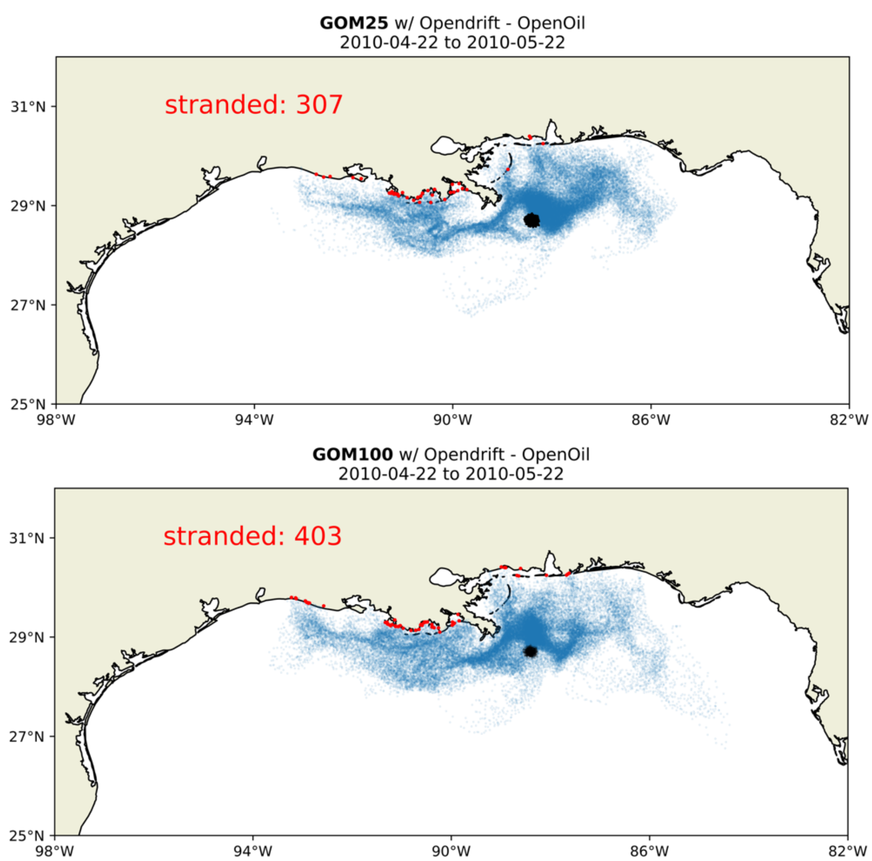

Figure 10: Oil particle positions from April 22, 2010 to May 22, 2010 (blue colors). The black dot represents the initial positions of 1000 oil particles in a 5km radius at the Deepwater Horizon location (28.7°N, 88.4°W), using the velocity fields from GOM25 (top) and GOM100 (bottom).The red dots represent oil particles that are stranded on the shore.

5. **Summary and conclusions**

In this paper, the importance of model horizontal resolution in identifying the nature of mixing and dispersion was evaluated by comparing two data-assimilative, high-resolution simulations (1/25° - 4km and 1/100° - 1km), the latter being submesoscale-resolving. By employing both Eulerian and Lagrangian metrics, upper-ocean differences between the mesoscale- and submesoscale-resolving simulations are examined and the nature of mixing in both simulations is identified by conducting Lagrangian experiments to track the generation of Lagrangian Coherent Structures (LCSs) and their associated transport barriers.

The added value of the increased resolution was first explored by comparing surface velocity fields from both simulations with independent drifter observations. Drifter trajectories from various experiments between 2013 and 2020 were used, separated by drifter type: CARTHE, SVP, and CODE drifters. In all three comparisons, GOM100 yielded reduced RMSEs after filtering out the unconstrained scales in the model (D'Addezio et al., 2019; Jacobs et al., 2019; Jacobs et al., 2021). This supports the hypothesis that higher resolution models prove value-added and that valuable information can be extracted from both constrained (large-scale and mesoscale) and unconstrained (small-scale) scales. There is higher kinetic energy in the larger wavenumbers in GOM100 and the slopes of the kinetic energy spectra are shallower (~-3) than in GOM25, a consequence of the submesoscale activity in GOM100, with small-scale vortices, meanders, and filaments that are not present/resolved in GOM25.

To investigate differences in mixing and dispersion between the two simulations, we calculated backward-time Finite-time Lyapunov exponents (FTLEs) and their associated Lagrangian Coherent Structures (LCSs). FTLEs measure the finite-time separation rate of nearby fluid particles and the average rate of stretching about a particle trajectory. Curvature ridges of backward in time FTLEs are indicators of attracting LCSs, that act as accumulation and convergence regions, which drive the fate of dispersants in the ocean. The boundaries of LCSs mark transport barriers that separate fluids with different advection properties that are approximately immiscible during the time interval of FTLE calculation. To calculate FTLEs, we first conducted 2-D particle experiments every 10 days starting on January 1, 2010 until the end of 2010, in the northeastern GoM, a region characterized by high submesoscale activity. GOM100 exhibited higher separation rates, with more intricate LCSs, demonstrating that mixing is more vigorous in the submesoscale-resolving simulation. The asymmetry of the PDFs of FTLEs in both experiments further suggests that chaotic advection dominates over turbulent mixing at the surface, although lower heterogeneity was detected in GOM100. The positive skewness of the PDFs of FTLEs in both simulations thus indicates that mixing induced by LCSs is mainly independent of horizontal resolution, as opposed to symmetrical PDFs that would imply mixing is mainly turbulent and dependent on horizontal resolution. The generation of more complex LCSs in the submesoscale-resolving simulation related to coherent eddies and fronts that are not resolved in the mesoscale-resolving one, highlights the significance of the horizontal resolution increase in numerical modeling.

Finally, the impact of resolution was explored by comparing the spread of oil particle trajectories in both simulations, initialized at the location of the 2010 Deepwater Horizon oil spill. The trajectories are clearly impacted by the horizontal resolution increase, with more oil particles reaching the coastlines of the northern GoM if advected using surface velocities from the submesoscale-resolving simulation. Further investigation of these patterns, alongside available observational data will provide more insight on the importance of resolving finer scales for monitoring such events. This result further underlies that Lagrangian flow applications, such as predicting the fate of dispersants, can benefit from progress in numerical modeling.

It is worth noting that future work is needed to assess mixing and dispersion at depth; identifying differences in the 3-D structure of the complex GoM dynamics would yield a more complete analysis of the impact of horizontal resolution in various depths, below the direct effect of data assimilation in the system. Finally, 3-D oil particle simulations, alongside FTLE calculations at the appropriate time scales for such applications, would be beneficial to provide additional results on the value of the added resolution on the representation of the GoM dynamics from a Lagrangian perspective.

Acknowledgements

We acknowledge support from the Bureau of Ocean Energy Management under award number M20AC10020-40 and the Gulf Research Program of the National Academies of Sciences, Engineering, and Medicine under award number 2000013149. The content is solely the responsibility of the authors and does not necessarily represent the official views of the Bureau of Ocean Energy Management, the Gulf Research Program, or the National Academies of Sciences, Engineering, and Medicine.

References

Allshouse, M.R., Peacock, T., 2015. Refining finite-time Lyapunov exponent ridges and the challenges of classifying them. Chaos Interdiscip. J. Nonlinear Sci. 25, 087410. https://doi.org/10.1063/1.4928210

Barkan, R., McWilliams, J.C., Molemaker, M.J., Choi, J., Srinivasan, K., Shchepetkin, A.F., Bracco, A., 2017a. Submesoscale Dynamics in the Northern Gulf of Mexico. Part II: Temperature–Salinity Relations and Cross-Shelf Transport Processes. J. Phys. Oceanogr. 47, 2347–2360. https://doi.org/10.1175/JPO-D-17-0040.1

Barkan, R., McWilliams, J.C., Shchepetkin, A.F., Molemaker, M.J., Renault, L., Bracco, A., Choi, J., 2017b. Submesoscale Dynamics in the Northern Gulf of Mexico. Part I: Regional and Seasonal Characterization and the Role of River Outflow. J. Phys. Oceanogr. 47, 2325–2346. https://doi.org/10.1175/JPO-D-17-0035.1

Beron-Vera, F.J., 2010. Mixing by low- and high-resolution surface geostrophic currents. J. Geophys. Res. Oceans 115, 2009JC006006. https://doi.org/10.1029/2009JC006006

Beron-Vera, F.J., LaCasce, J.H., 2016. Statistics of Simulated and Observed Pair Separations in the Gulf of Mexico. J. Phys. Oceanogr. 46, 2183–2199. https://doi.org/10.1175/JPO-D-15-0127.1

Beron-Vera, F.J., Olascoaga, M.J., 2009. An Assessment of the Importance of Chaotic Stirring and Turbulent Mixing on the West Florida Shelf. J. Phys. Oceanogr. 39, 1743–1755. https://doi.org/10.1175/2009JPO4046.1

Beron-Vera, F.J., Olascoaga, M.J., Goni, G.J., 2008. Oceanic mesoscale eddies as revealed by Lagrangian coherent structures: OCEANIC MESOSCALE EDDIES AS REVEALED BY LCSS. Geophys. Res. Lett. 35, n/a-n/a. https://doi.org/10.1029/2008GL033957

Bleck, R., 2002. An oceanic general circulation model framed in hybrid isopycnic-Cartesian coordinates. Ocean Model. 4, 55–88. https://doi.org/10.1016/S1463-5003(01)00012-9

Bracco, A., Liu, G., Sun, D., 2019. Mesoscale-submesoscale interactions in the Gulf of Mexico: From oil dispersion to climate. Chaos Solitons Fractals 119, 63–72. https://doi.org/10.1016/j.chaos.2018.12.012

Brown, M.G., Smith, K.B., 1991. Ocean stirring and chaotic low-order dynamics. Phys. Fluids Fluid Dyn. 3, 1186–1192. https://doi.org/10.1063/1.858047

Budyansky, M.V., Uleysky, M.Yu., Prants, S.V., 2007. Lagrangian coherent structures, transport and chaotic mixing in simple kinematic ocean models. Commun. Nonlinear Sci. Numer. Simul. 12, 31–44. https://doi.org/10.1016/j.cnsns.2006.01.008

Callies, J., Ferrari, R., Klymak, J.M., Gula, J., 2015. Seasonality in submesoscale turbulence. Nat. Commun. 6, 6862. https://doi.org/10.1038/ncomms7862

Capet, X., McWilliams, J.C., Molemaker, M.J., Shchepetkin, A.F., 2008a. Mesoscale to Submesoscale Transition in the California Current System. Part I: Flow Structure, Eddy Flux, and Observational Tests. J. Phys. Oceanogr. 38, 29–43. https://doi.org/10.1175/2007JPO3671.1

Capet, X., McWilliams, J.C., Molemaker, M.J., Shchepetkin, A.F., 2008b. Mesoscale to Submesoscale Transition in the California Current System. Part III: Energy Balance and Flux. J. Phys. Oceanogr. 38, 2256–2269. https://doi.org/10.1175/2008JPO3810.1

Capet, X., McWilliams, J.C., Molemaker, M.J., Shchepetkin, A.F., 2008c. Mesoscale to Submesoscale Transition in the California Current System. Part II: Frontal Processes. J. Phys. Oceanogr. 38, 44–64. https://doi.org/10.1175/2007JPO3672.1

Chassignet, E.P., Smith, L.T., Halliwell, G.R., Bleck, R., 2003. North Atlantic Simulations with the Hybrid Coordinate Ocean Model (HYCOM): Impact of the Vertical Coordinate Choice, Reference Pressure, and Thermobaricity. J. Phys. Oceanogr. 33, 2504–2526. https://doi.org/10.1175/1520-0485(2003)033<2504:NASWTH>2.0.CO;2

Choi, J., Bracco, A., Barkan, R., Shchepetkin, A.F., McWilliams, J.C., Molemaker, J.M., 2017. Submesoscale Dynamics in the Northern Gulf of Mexico. Part III: Lagrangian Implications. J. Phys. Oceanogr. 47, 2361–2376. https://doi.org/10.1175/JPO-D-17-0036.1

Cooper, M., Haines, K., 1996. Altimetric assimilation with water property conservation. J. Geophys. Res. Oceans 101, 1059–1077. https://doi.org/10.1029/95JC02902

D’Addezio, J.M., Smith, S., Jacobs, G.A., Helber, R.W., Rowley, C., Souopgui, I., Carrier, M.J., 2019. Quantifying wavelengths constrained by simulated SWOT observations in a submesoscale resolving ocean analysis/forecasting system. Ocean Model. 135, 40–55. https://doi.org/10.1016/j.ocemod.2019.02.001

D'Asaro, E., Lee, C., Rainville, L., Harcourt, R., Thomas, L., 2011. Enhanced Turbulence and Energy Dissipation at Ocean Fronts. Science 332, 318–322. https://doi.org/10.1126/science.1201515

Davis, R.E., 1985. Drifter observations of coastal surface currents during CODE: The method and descriptive view. J. Geophys. Res. Oceans 90, 4741–4755. https://doi.org/10.1029/JC090iC03p04741

Delandmeter, P., Van Sebille, E., 2019. The Parcels v2.0 Lagrangian framework: new field interpolation schemes. Geosci. Model Dev. 12, 3571–3584. https://doi.org/10.5194/gmd-12-3571-2019

Dorandeu, J., Le Traon, P.Y., 1999. Effects of Global Mean Atmospheric Pressure Variations on Mean Sea Level Changes from TOPEX/Poseidon. J. Atmospheric Ocean. Technol. 16, 1279–1283. https://doi.org/10.1175/1520-0426(1999)016<1279:EOGMAP>2.0.CO;2

Egbert, G.D., Erofeeva, S.Y., 2002. Efficient Inverse Modeling of Barotropic Ocean Tides. J. Atmospheric Ocean. Technol. 19, 183–204. https://doi.org/10.1175/1520-0426(2002)019<0183:EIMOBO>2.0.CO;2

Elipot, S., Lumpkin, R., Perez, R.C., Lilly, J.M., Early, J.J., Sykulski, A.M., 2016. A global surface drifter data set at hourly resolution. J. Geophys. Res. Oceans 121, 2937–2966. https://doi.org/10.1002/2016JC011716

Evensen, G., 2003. The Ensemble Kalman Filter: theoretical formulation and practical implementation. Ocean Dyn. 53, 343–367. https://doi.org/10.1007/s10236-003-0036-9

Farazmand, M., Haller, G., 2013. Attracting and repelling Lagrangian coherent structures from a single computation. Chaos Interdiscip. J. Nonlinear Sci. 23, 023101. https://doi.org/10.1063/1.4800210

Haller, G., 2002. Lagrangian coherent structures from approximate velocity data. Phys. Fluids 14, 1851–1861. https://doi.org/10.1063/1.1477449

Haller, G., 2001a. Distinguished material surfaces and coherent structures in three-dimensional fluid flows. Phys. Nonlinear Phenom. 149, 248–277. https://doi.org/10.1016/S0167-2789(00)00199-8

Haller, G., 2001b. Lagrangian structures and the rate of strain in a partition of two-dimensional turbulence. Phys. Fluids 13, 3365–3385. https://doi.org/10.1063/1.1403336

Haller, G., Yuan, G., 2000. Lagrangian coherent structures and mixing in two-dimensional turbulence. Phys. Nonlinear Phenom. 147, 352–370. https://doi.org/10.1016/S0167-2789(00)00142-1

Haza, A.C., D'Asaro, E., Chang, H., Chen, S., Curcic, M., Guigand, C., Huntley, H.S., Jacobs, G., Novelli, G., Özgökmen, T.M., Poje, A.C., Ryan, E., Shcherbina, A., 2018. Drogue-Loss Detection for Surface Drifters during the Lagrangian Submesoscale Experiment (LASER). J. Atmospheric Ocean. Technol. 35, 705–725. https://doi.org/10.1175/JTECH-D-17-0143.1

Jacobs, G., D'Addezio, J.M., Ngodock, H., Souopgui, I., 2021. Observation and model resolution implications to ocean prediction. Ocean Model. 159, 101760. https://doi.org/10.1016/j.ocemod.2021.101760

Jacobs, G.A., D'Addezio, J.M., Bartels, B., Spence, P.L., 2021. Constrained scales in ocean forecasting. Adv. Space Res. 68, 746–761. https://doi.org/10.1016/j.asr.2019.09.018

Klein, P., Hua, B.L., Lapeyre, G., Capet, X., Le Gentil, S., Sasaki, H., 2008. Upper Ocean Turbulence from High-Resolution 3D Simulations. J. Phys. Oceanogr. 38, 1748–1763. https://doi.org/10.1175/2007JPO3773.1

Koshel', K.V., Prants, S.V., 2006. Chaotic advection in the ocean. Phys.-Uspekhi 49, 1151–1178. https://doi.org/10.1070/PU2006v049n11ABEH006066

Le Traon, P. -Y., Ogor, F., 1998. ERS-1/2 orbit improvement using TOPEX/POSEIDON: The 2 cm challenge. J. Geophys. Res. Oceans 103, 8045–8057. https://doi.org/10.1029/97JC01917

Lilly, J.M., Pérez-Brunius, P., 2021. A gridded surface current product for the Gulf of Mexico from consolidated drifter measurements. Earth Syst. Sci. Data 13, 645–669. https://doi.org/10.5194/essd-13-645-2021

Liu, G., Bracco, A., Passow, U., 2018. The influence of mesoscale and submesoscale circulation on sinking particles in the northern Gulf of Mexico. Elem. Sci. Anthr. 6, 36. https://doi.org/10.1525/elementa.292

Liu, G., Bracco, A., Sitar, A., 2021. Submesoscale Mixing Across the Mixed Layer in the Gulf of Mexico. Front. Mar. Sci. 8, 615066. https://doi.org/10.3389/fmars.2021.615066

Liu, Y., Weisberg, R.H., Hu, C., Zheng, L., 2011. Tracking the Deepwater Horizon Oil Spill: A Modeling Perspective. Eos Trans. Am. Geophys. Union 92, 45–46. https://doi.org/10.1029/2011EO060001

Lumpkin, R., Pazos, M., 2007. Measuring surface currents with Surface Velocity Program drifters: the instrument, its data, and some recent results, in: Griffa, A., Kirwan, Jr., A.D., Mariano, A.J., Özgökmen, T., Rossby, H.T. (Eds.), Lagrangian Analysis and Prediction of Coastal and Ocean Dynamics. Cambridge University Press, pp. 39–67. https://doi.org/10.1017/CBO9780511535901.003

Luo, H., Bracco, A., Cardona, Y., McWilliams, J.C., 2016. Submesoscale circulation in the northern Gulf of Mexico: Surface processes and the impact of the freshwater river input. Ocean Model. 101, 68–82. https://doi.org/10.1016/j.ocemod.2016.03.003

M. P. Perez, G., Vidale, P.L., Klingaman, N.P., C. M. Martin, T., 2020. Atmospheric convergence zones stemming from large-scale mixing (preprint). Links between the atmospheric water cycle and weather systems. https://doi.org/10.5194/wcd-2020-57

Mahadevan, A., Tandon, A., 2006. An analysis of mechanisms for submesoscale vertical motion at ocean fronts. Ocean Model. 14, 241–256. https://doi.org/10.1016/j.ocemod.2006.05.006

McWilliams, J.C., 2016. Submesoscale currents in the ocean. Proc. R. Soc. Math. Phys. Eng. Sci. 472, 20160117. https://doi.org/10.1098/rspa.2016.0117

Molemaker, M.J., McWilliams, J.C., Yavneh, I., 2005. Baroclinic Instability and Loss of Balance. J. Phys. Oceanogr. 35, 1505–1517. https://doi.org/10.1175/JPO2770.1

Novelli, G., Guigand, C.M., Cousin, C., Ryan, E.H., Laxague, N.J.M., Dai, H., Haus, B.K., Özgökmen, T.M., 2017. A Biodegradable Surface Drifter for Ocean Sampling on a Massive Scale. J. Atmospheric Ocean. Technol. 34, 2509–2532. https://doi.org/10.1175/JTECH-D-17-0055.1

Oke, P.R., Allen, J.S., Miller, R.N., Egbert, G.D., Kosro, P.M., 2002. Assimilation of surface velocity data into a primitive equation coastal ocean model. J. Geophys. Res. Oceans 107. https://doi.org/10.1029/2000JC000511

Olascoaga, M.J., 2010. Isolation on the West Florida Shelf with implications for red tides and pollutant dispersal in the Gulf of Mexico. Nonlinear Process. Geophys. 17, 685–696. https://doi.org/10.5194/npg-17-685-2010

Olascoaga, M.J., Haller, G., 2012. Forecasting sudden changes in environmental pollution patterns. Proc. Natl. Acad. Sci. 109, 4738–4743. https://doi.org/10.1073/pnas.1118574109

Olascoaga, M.J., Rypina, I.I., Brown, M.G., Beron-Vera, F.J., Koçak, H., Brand, L.E., Halliwell, G.R., Shay, L.K., 2006. Persistent transport barrier on the West Florida Shelf. Geophys. Res. Lett. 33, 2006GL027800. https://doi.org/10.1029/2006GL027800

Özgökmen, T.M., Boufadel, M., Carlson, D.F., Cousin, C., Guigand, C., Haus, B.K., Horstmann, J., Lund, B., Molemaker, J., Novelli, G., 2018. Technological Advances for Ocean Surface Measurements by the Consortium for Advanced Research on Transport of Hydrocarbons in the Environment (CARTHE). Mar. Technol. Soc. J. 52, 71–76. https://doi.org/10.4031/MTSJ.52.6.11

Pierrehumbert, R.T., 1991. Large-scale horizontal mixing in planetary atmospheres. Phys. Fluids Fluid Dyn. 3, 1250–1260. https://doi.org/10.1063/1.858053

Poje, A.C., Özgökmen, T.M., Lipphardt, B.L., Haus, B.K., Ryan, E.H., Haza, A.C., Jacobs, G.A., Reniers, A.J.H.M., Olascoaga, M.J., Novelli, G., Griffa, A., Beron-Vera, F.J., Chen, S.S., Coelho, E., Hogan, P.J., Kirwan, A.D., Huntley, H.S., Mariano, A.J., 2014. Submesoscale dispersion in the vicinity of the *Deepwater Horizon* spill. Proc. Natl. Acad. Sci. 111, 12693–12698. https://doi.org/10.1073/pnas.1402452111

Shadden, S.C., Lekien, F., Marsden, J.E., 2005. Definition and properties of Lagrangian coherent structures from finite-time Lyapunov exponents in two-dimensional aperiodic flows. Phys. Nonlinear Phenom. 212, 271–304. https://doi.org/10.1016/j.physd.2005.10.007

Sinha, A., Balwada, D., Tarshish, N., Abernathey, R., 2019. Modulation of Lateral Transport by Submesoscale Flows and Inertia-Gravity Waves. J. Adv. Model. Earth Syst. 11, 1039–1065. https://doi.org/10.1029/2018MS001508

Srinivasan, A., Chin, T.M., Chassignet, E.P., Iskandarani, M., Groves, N., 2022. A Statistical Interpolation Code for Ocean Analysis and Forecasting. J. Atmospheric Ocean. Technol. 39, 367–386. https://doi.org/10.1175/JTECH-D-21-0033.1

Thomas, L.N., Tandon, A., Mahadevan, A., 2008. Submesoscale processes and dynamics, in: Hecht, M.W., Hasumi, H. (Eds.), Geophysical Monograph Series. American Geophysical Union, Washington, D. C., pp. 17–38. https://doi.org/10.1029/177GM04

Thompson, A.F., Lazar, A., Buckingham, C., Naveira Garabato, A.C., Damerell, G.M., Heywood, K.J., 2016. Open-Ocean Submesoscale Motions: A Full Seasonal Cycle of Mixed Layer

Instabilities from Gliders. J. Phys. Oceanogr. 46, 1285–1307. https://doi.org/10.1175/JPO-D-15-0170.1

Waugh, D.W., Abraham, E.R., 2008. Stirring in the global surface ocean. Geophys. Res. Lett. 35, 2008GL035526. https://doi.org/10.1029/2008GL035526

Yang, H., Weisberg, R.H., Niiler, P.P., Sturges, W., Johnson, W., 1999. Lagrangian circulation and forbidden zone on the West Florida Shelf. Cont. Shelf Res. 19, 1221–1245. https://doi.org/10.1016/S0278-4343(99)00021-7

Yang, Y., McWilliams, J.C., San Liang, X., Zhang, H., Weisberg, R.H., Liu, Y., Menemenlis, D., 2021. Spatial and Temporal Characteristics of the Submesoscale Energetics in the Gulf of Mexico. J. Phys. Oceanogr. 51, 475–489. https://doi.org/10.1175/JPO-D-20-0247.1

Zhong, Y., Bracco, A., 2013. Submesoscale impacts on horizontal and vertical transport in the Gulf of Mexico: Submesoscale Transport in Gulf of Mexico. J. Geophys. Res. Oceans 118, 5651–5668. https://doi.org/10.1002/jgrc.20402